

CO on a Rh/Fe₃O₄ single-atom catalyst: high-resolution infrared spectroscopy and near-ambient-pressure scanning tunnelling microscopy

Nail El Hocine Barama,^a Chunlei Wang,^a Panukorn Sombut,^a David Rath,^a Adam Lagin,^a Martin Ormoš,^b Lena Puntscher,^a Faith J. Lewis,^a Zdeněk Jakub,^{a,c} Florian Kraushofer,^a Moritz Eder,^a Matthias Meier,^d Michael Schmid,^a Ulrike Diebold,^a Cesare Franchini,^{d,e} Peter Matvija,^b Jiří Pavelec*^a and Gareth S. Parkinson^a

Infrared reflection absorption spectroscopy (IRAS) offers a powerful route to bridging the materials and pressure gaps between surface science and powder catalysis. Using a newly developed IRAS setup optimised for dielectric single crystals, we investigate CO adsorption on the model single-atom catalyst Rh/Fe₃O₄(001). IRAS resolves three species: monocarbonyls at twofold coordinated Rh₁ sites, monocarbonyls at fivefold coordinated Rh sites, and gem-dicarbonyls at twofold coordinated Rh₁ sites. Under ultra-high vacuum (UHV) conditions, Rh₁CO monocarbonyl species dominate. Rh₁(CO)₂ gem-dicarbonyl formation is kinetically hindered and occurs predominantly through CO-induced dissociation of Rh₂ dimers rather than sequential CO adsorption. The sequential-adsorption pathway to Rh₁(CO)₂ becomes accessible at millibar CO pressures as evidenced by near-ambient-pressure scanning tunnelling microscopy (NAP-STM). These findings validate the kinetic picture inferred from UHV measurements and computational modelling and link the UHV behaviour to that expected under realistic reaction conditions. Assignments of the vibrational frequencies to individual species rely on isotopic labelling, thermal treatments, and a review of previous SPM, XPS, and TPD data, supported by density functional theory (DFT)-based calculations. While theory provides qualitative insight, such as the instability of dicarbonyls on fivefold coordinated Rh atoms, it does not yet reproduce experimental frequencies quantitatively and is sensitive to the computational parameters, highlighting the need for robust experimental benchmarks. The spectroscopic fingerprints established here provide a reliable foundation for identifying Rh coordination environments in oxide-supported single-atom catalysts.

1. Introduction

Infrared (IR) spectroscopy is one of the most powerful techniques in heterogeneous catalysis and is the most widely used among optical spectroscopies in this field,¹ as it can be used to monitor the evolution of surface-bound intermediates under operando conditions.^{2–5} Furthermore, different implementations of this technique enable its application to diverse types of samples, ranging from powders, investigated by diffuse reflectance infrared Fourier transform spectroscopy (DRIFTS), to flat single crystals, studied by infrared reflection absorption spectroscopy (IRAS or IRRAS). As a result, IR studies on powder-supported catalysts have provided invaluable insight into reaction mechanisms. Moreover, CO titration is frequently used to study the properties of active sites because the CO-stretch frequency is sensitive to the local coordination environment.^{6–14}

Oxide-supported Rh compounds are key materials in heterogeneous catalysis, for example, in automotive emission control and various selective hydrogenation and oxidation reactions.^{15–19} Accordingly, IR absorption studies of CO adsorption on Rh-supported powder catalysts have attracted attention for decades. The earliest report dates back to 1957, when Yang and Garland investigated the sintering of dispersed Rh and assigned the resulting CO vibrational doublet to a single Rh adsorption site.²⁰ Since then, numerous studies have employed IR spectroscopy to investigate Rh-based powder catalysts, revealing both the complexity of CO adsorption and the diversity of the resulting surface species.^{18,21–28} However, the structural complexity and heterogeneity of such catalysts make it difficult to unambiguously link a given vibrational feature to a specific atomic site. The coexistence of multiple adsorption geometries and the dynamic restructuring of active sites under reaction conditions further complicate interpretation, as highlighted in a recent review on IR characterisation of isolated atoms and nanoparticles.²⁹

The surface-science approach enables experiments on well-defined catalytic model systems under tightly controlled UHV conditions. This includes single-atom catalysts (SACs) supported on single-crystal oxides, which provide a powerful platform for disentangling these complexities. Such model systems allow a direct correlation between atomic structure, electronic configuration, and vibrational signatures, whose frequencies are also, in principle, straightforward to calculate using DFT. Nonetheless, applying IRAS to metal oxide single crystals, the predominant support materials in catalysis, is challenging. The optimal incidence angles required to enhance adsorbate signals often coincide with regions of low infrared reflectivity, thereby drastically reducing signal intensity.³⁰ As a result, IRAS studies on metal oxides remain scarce. A common workaround is to grow thin oxide films on metal substrates to benefit from the high reflectivity of metals;^{31–34} however, this strategy limits the accessible facets and may introduce structural or electronic deviations from those of bulk single crystals or conventional oxide powders. Overcoming these challenges for metal oxide single crystals is particularly important, as IRAS offers the unique combination of surface sensitivity and compatibility with elevated pressures, making it well suited to bridge the pressure gap between model catalysts and practical materials.^{35,36}

While UHV-based surface-science studies allow insights at the atomic scale, they often cannot access adsorption pathways that are kinetically hindered at low pressure. In particular, sequential adsorption steps that require short-lived intermediate geometries may be strongly suppressed under UHV conditions even when thermodynamically favourable. To assess how the CO adsorption mechanism evolves with pressure, and to test whether additional pathways become accessible under catalytic conditions, it is essential to complement UHV spectroscopy on well-investigated model systems with techniques capable of operating at elevated gas pressures. The Fe₃O₄(001) surface represents such a model system. It exhibits a well-investigated subsurface cation-vacancy (SCV) reconstruction,³⁷ which exposes a periodic array of surface oxygen atoms that can stabilise isolated metal adatoms. This makes Fe₃O₄(001) an ideal platform for SAC studies, and a wide range of metals, including Rh, have been

systematically explored on this surface.^{38–41} In the case of Rh, previous surface-science work has established how preparation conditions such as adsorption temperature, annealing, and coverage determine whether Rh occurs as isolated adatoms, substitutional species, or small clusters.^{39,42–45} The interaction of CO with these Rh species has also been extensively characterised using experiments and DFT calculations, providing a detailed picture of the resulting adsorption geometries.^{42,46,47} As a result, Rh/Fe₃O₄(001) is one of the best-characterised model systems for oxide-supported Rh catalysts, offering atomic-level structural control that is difficult to achieve on powders. Investigating this system by IRAS is thus of particular interest, as it offers a direct link between fundamental surface-science insights and the behaviour of applied, high-surface-area catalysts.

In this work, we present a high-resolution IRAS investigation of CO adsorption on the model Rh/Fe₃O₄(001) single-atom catalyst. By combining isotope-substitution experiments (¹²CO, ¹³CO, and mixed ¹²CO/¹³CO) with precise control over Rh coverage and surface preparation, we assign each observed vibrational feature unambiguously to a specific Rh coordination environment. DFT calculations capture the qualitative trends, but do not reproduce all vibrational frequencies quantitatively. Our IRAS study, therefore, provides a set of reference spectra for oxide-supported single-atom catalysts, offering a firm foundation for interpreting CO vibrational signatures in practical Rh catalysts and for evaluating theoretical predictions. To probe the pressure dependence of the CO adsorption mechanism, we further complemented the UHV-IRAS measurements with NAP-STM, which allowed us to determine whether the sequential-adsorption pathway to Rh₁(CO)₂, kinetically inaccessible in UHV, becomes accessible under mbar CO exposures.

2. Methods

IRAS measurements were performed using a newly developed setup optimised to maximise the signal-to-noise ratio for metal oxide surfaces⁴⁸. All spectra were acquired with a resolution of 4 cm⁻¹ and averaged over 4000 scans, corresponding to an acquisition time of approximately 20 min per spectrum. The measurements were conducted with p-polarised light at non-grazing incidence angles between 55° and 74°, a range optimised for the Fe₃O₄(001) surface to enhance peak intensity. The spectrometer used in the IRAS setup is a Bruker VERTEX 80v. The entire system is housed within a custom-built UHV chamber designed for chemical reactivity studies, operating at a base pressure below 1 × 10⁻¹⁰ mbar.⁴⁹ The chamber is equipped with a triple-pocket electron-beam evaporator for metal deposition and a temperature-stabilised quartz-crystal microbalance (QCM) used to monitor and calibrate the Rh deposition rate. For Fe₃O₄(001), one monolayer (1 ML) is defined as one Rh atom per ($\sqrt{2} \times \sqrt{2}$)R45° unit cell, corresponding to 1.42 × 10¹⁴ atoms per cm². Carbon monoxide was dosed using a home-built molecular beam source that provides uniform exposure over a well-defined ≈3.5 mm diameter area on the sample surface.^{49,50} The UHV chamber is equipped with several complementary surface-science techniques, including X-ray photoelectron spectroscopy (XPS), ultraviolet photoelectron spectroscopy (UPS), temperature-programmed desorption (TPD), low-energy electron diffraction (LEED), and low-energy ion scattering (LEIS). In the present work, XPS was employed to verify surface cleanliness and confirm Rh coverages. XPS spectra were

recorded using a monochromatized Al/Ag twin-anode X-ray source (SPECS XR50 M, FOCUS 500) and a hemispherical analyser (SPECS Phoibos 150) with Al K α radiation.

UHV scanning tunnelling microscopy (STM) measurements were performed on a separate Fe₃O₄(001) sample in an independent UHV system consisting of a preparation chamber ($p < 1 \times 10^{-10}$ mbar) and an analysis chamber ($p < 7 \times 10^{-11}$ mbar). The STM (Omicron μ -STM) was operated at room temperature in constant-current mode using electrochemically etched tungsten tips. Further details of this setup are provided in previous papers.^{38,51,52}

Non-contact atomic force microscopy (nc-AFM) measurements were carried out on an additional Fe₃O₄(001) sample in a dedicated UHV chamber ($p < 1 \times 10^{-10}$ mbar) using a qPlus sensor⁵³ ($f_0 = 31.8$ kHz, $k = 1800$ N/m, $Q \approx 10\,000$) with an electrochemically etched tungsten tip. The CO-tip functionalization was spontaneously formed during STM scanning or mild bias pulsing above Rh–CO species, similarly to previous reports.⁴⁰

Near-ambient-pressure measurements were performed in collaboration with the Nanomaterials Group at Charles University in Prague. The system consists of a UHV preparation chamber equipped with XPS, an electron-beam evaporator, an electron beam heating stage, and an oxygen supply, connected via a transfer line to a second chamber housing an Aarhus NAP-STM/AFM microscope. The base pressure was 1×10^{-9} mbar in the preparation chamber and 1×10^{-10} mbar in the STM/AFM chamber. CO (Linde, 99.997%) was introduced into the STM/AFM enclosure via a leak valve equipped with a cryogenic (LN₂-cooled) filter. Near-ambient pressures in the range of 1–10 mbar were applied at room temperature and monitored using a calibrated Pirani gauge. STM images were acquired in constant-current mode under stable CO pressure, with typical tunnelling conditions of +0.7–1.2 V sample bias and 20–50 pA. After the NAP-STM measurements, the high-pressure cell was pumped back to UHV, and the sample was imaged again to confirm that no pressure- or tip-induced morphological changes had occurred.

All samples used in this study were natural Fe₃O₄(001) single crystals obtained from SurfaceNet GmbH. Surface preparation consisted of repeated cycles of Ne⁺ (or Ar⁺, depending on the chamber) ion sputtering at 300 K (1 keV, 15 min) followed by annealing under UHV at 900 K for 15 min. Every second annealing cycle was performed in an oxygen atmosphere ($p(O_2) = 3 \times 10^{-7}$ mbar, 20 min) to prevent reducing the sample.

VASP was used for all DFT calculations with the PAW method and a 550 eV plane-wave cutoff.^{54–56} Electronic exchange-correlation was treated using the GGA-PBE functional with D3 dispersion corrections (Becke-Johnson damping), and strong correlation of Fe 3d states was described with $U_{\text{eff}} = 3.61$ eV.^{57–60} Electronic self-consistency and ionic-relaxation were converged to 10^{−6} eV and 0.02 eV/Å, respectively. The Fe₃O₄(001) surface was modelled by an asymmetric 13-layer slab (7 octahedral and 6 tetrahedral Fe layers) in a (2 $\sqrt{2}$ ×2 $\sqrt{2}$)R45° supercell, with the top 4 layers relaxed, the bottom 9 fixed, Γ -point sampling only, and 14 Å of

vacuum.⁴⁶ CO vibrational frequencies were computed in the harmonic approximation using finite differences. Motivated by the use of DFT+U to mitigate self-interaction errors in localised d states, we also examined the effect of applying a Hubbard U to the Rh 4d states, using the same U_{eff} value as for the Fe 3d states, on the calculated CO stretching frequencies. The computed CO stretching vibrational frequency for adsorbed CO on the Rh/Fe₃O₄(001) was scaled by the factor $\lambda = \nu_{\text{CO}_{\text{gas}}}^{\text{exp}} / \nu_{\text{CO}_{\text{gas}}}^{\text{cal}}$ to compensate for the systematic DFT errors, where $\nu_{\text{CO}_{\text{gas}}}^{\text{exp}}$ is the frequency of an isolated CO molecule in the gas phase.⁶¹

3. Summary of results from our previous studies

The adsorption of Rh on Fe₃O₄(001) in the low-coverage regime has been comprehensively characterised in our previous studies.^{42,46,47} Additional work by Sharp *et al.* further refined this picture by mapping the distribution of Rh species over a wide range of coverages and annealing temperatures.³⁹ In the present study, we focus on low Rh coverages (< 0.5 ML) deposited at room temperature, where isolated Rh₁ adatoms dominate. These adatoms are twofold coordinated to surface oxygen atoms within the SCV reconstruction and appear in STM images as bright protrusions centred between the rows of octahedrally coordinated Fe atoms (Fe_{oct}).⁴⁷ The Rh₁ adsorption energy at this site was calculated to be $E_{\text{ads}} = -4.42$ eV.⁴⁶ Occasionally, Rh₁ adatoms pair to form Rh₂ dimers, which appear as slightly elongated protrusions in STM. At room temperature, the dimers switch between two equivalent configurations by moving parallel to the Fe_{oct}.^{42,46} DFT calculations indicate that these dimers are thermodynamically preferred over two isolated adatoms by approximately 0.19 eV, but kinetic barriers prevent pairing of all Rh₁ adatoms at room temperature. Dimers account for approximately 12 % of the total Rh population at an initial coverage of 0.2 ML. In addition to adatoms and dimers, some Rh atoms substitute surface/subsurface Fe_{oct} sites within the spinel structure to form fivefold (Rh_{5-fold}) or sixfold (Rh_{6-fold}) coordinated Rh sites.⁴² These substitutional Rh atoms are stabilised relative to the Rh₁ adatom by 0.67 eV for the fivefold configuration and by 1.10 eV for the sixfold configuration. Only the surface Rh_{5-fold} species are relevant to our CO adsorption studies here. Although these substitutional Rh atoms are already present in small quantities after room-temperature deposition, annealing above ≈ 400 K drives a substantial fraction of Rh₁ adatoms into the more highly coordinated Rh_{5-fold} sites.

Figure 1 summarises the three principal CO adsorption configurations on Rh sites observed after CO exposure on a low-coverage Rh/Fe₃O₄(001) surface.^{42,46} Figure 1a presents an STM image (top) and a nc-AFM image (bottom) of the same surface region, both recorded at 78 K using a CO-terminated tip after CO exposure. The most abundant species are Rh₁CO monocarbonyls (highlighted by cyan arrows).⁴⁶ Upon CO adsorption, the Rh₁ adatom sinks slightly into the surface and forms an additional bond with one of the two equivalent subsurface oxygen atoms, forming a pseudo-square-planar geometry tilted away from the surface normal. The weak bond to the subsurface oxygen enables rapid switching between two equivalent configurations along the [110] direction. As a result, the species appear as faint double

protrusions in nc-AFM and as elongated features in STM. The corresponding structural model and calculated adsorption energy are shown in Figure 1b.

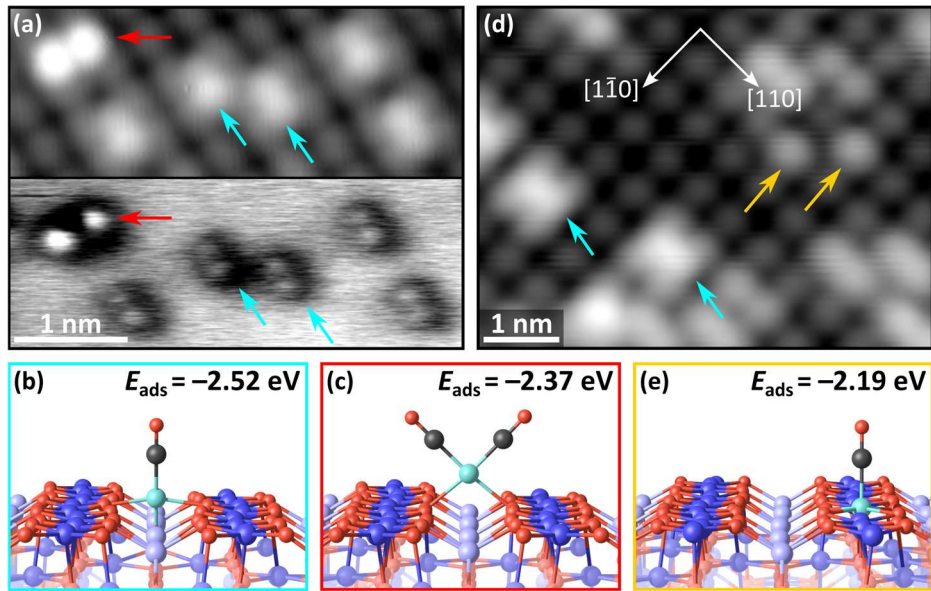


Figure 1. CO adsorption configurations on Rh/Fe₃O₄(001). (a) STM (top) and nc-AFM (bottom) images acquired at 78 K after CO exposure on low-coverage Rh/Fe₃O₄(001). Cyan arrows mark monocarbonyls on twofold Rh₁ sites, and red arrows indicate gem-dicarbonyls on twofold Rh₁ sites. (b) DFT model of the pseudo-square-planar geometry adopted by the Rh₁ monocarbonyl. The CO is not vertical but tilted towards the viewer by $\approx 20^\circ$. (c) DFT model of the gem-dicarbonyl on a twofold Rh₁ site. (d) STM image extracted from a movie recorded during CO exposure on 0.2 ML Rh/Fe₃O₄(001). Yellow arrows mark CO adsorbed on Rh₅-fold atoms substituting Fe_{oct} sites. (e) DFT model of CO adsorbed on a Rh₅-fold site. Adsorption energies are based on PBE-D3 with $U_{Rh} = 0$.

In addition, the bright double-lobed protrusions oriented perpendicular to the Fe_{oct} rows (red arrows in Figure 1a) are assigned to Rh₁(CO)₂ gem-dicarbonyl species. As demonstrated by Wang *et al.*,⁴⁶ these dicarbonyls form almost exclusively through CO-induced dissociation of the minority Rh₂ dimers present on the surface under UHV conditions. This process was captured in sequential STM images, and DFT calculations revealed that, upon CO exposure, the Rh₂ dimers pass through an unstable intermediate Rh₂(CO)₃ configuration, which subsequently dissociates to produce one monocarbonyl Rh₁CO and one gem-dicarbonyl Rh₁(CO)₂. Although the Rh₁(CO)₂ configuration is thermodynamically stable (average adsorption energy $E_{ads} = -2.37$ eV per CO with the PBE-D3 functional used in the current work; no U on Rh), sequential adsorption of two CO molecules on an isolated Rh₁ adatom was never observed in UHV. Our previous combined STM/DFT analysis suggested that this pathway requires the Rh₁CO to adopt a transient, sterically constrained geometry with an extremely low configurational probability. Since the Rh₁CO assumes this configuration only during a tiny fraction of the time ($< 10^{-8}$), adsorption of another CO during these short periods is extremely unlikely at UHV gas impingement rates.⁴⁶ This kinetic picture predicts that sufficiently high

CO pressures should enable the sequential-adsorption mechanism by dramatically increasing the rate at which CO molecules encounter Rh_1CO species in the required transient geometry. As shown in section 5, NAP-STM measurements presented in the current work indeed reveal that the sequential CO adsorption pathway becomes accessible under mbar CO pressures, providing direct experimental support for this kinetic interpretation. The structural model of $\text{Rh}_1(\text{CO})_2$ and the calculated adsorption energy per CO molecule are shown in Figure 1c.

CO can also adsorb on the substitutional $\text{Rh}_{5\text{-fold}}$ sites. In this case, DFT calculations indicate that gem-dicarbonyl formation is energetically unfavourable.⁴⁶ Only a single CO molecule can bind to a $\text{Rh}_{5\text{-fold}}$ atom, completing an octahedral coordination environment (Figure 1e). CO adsorption at these sites is significantly weaker ($E_{\text{ads}} = -2.19$ eV with PBE-D3, $U_{\text{Rh}} = 0$) than at the twofold coordinated Rh_1 sites ($E_{\text{ads}} = -2.52$ eV).⁴⁶ These calculations are in excellent agreement with experimental CO TPD experiments, where monocarbonyls on $\text{Rh}_{5\text{-fold}}$ lead to a desorption peak at around 410 K, notably lower than the desorption peak stemming from the twofold Rh_1 at 530 K.⁴² The STM image in Figure 1d is extracted from a movie recorded before and during CO exposure. The movie illustrates how twofold Rh_1 sites transform into elongated features upon CO adsorption (highlighted again by cyan arrows).⁴⁶ In contrast, the $\text{Rh}_{5\text{-fold}}$ sites exhibit only a subtle change in contrast upon CO adsorption and are marked by yellow arrows. Owing to their low concentration under the present deposition conditions (temperature and coverage), these species are observed only rarely in STM. Nevertheless, they are expected to give distinct signatures in the infrared spectra, as IRAS is very sensitive to dipole moments normal to the surface. Together, these three configurations—monocarbonyls on twofold Rh_1 , gem-dicarbonyls on twofold Rh_1 , and monocarbonyls on $\text{Rh}_{5\text{-fold}}$ —constitute the structural basis for interpreting the IRAS spectra discussed in section 4. Their distinct adsorption geometries and adsorption energies are expected to produce characteristic shifts in the CO stretching frequencies that allow each configuration to be distinguished spectroscopically, and they represent the three relevant Rh–CO states from which the kinetic behaviour under different CO pressures emerges. Section 5 provides a direct NAP-STM test of this kinetic picture.

4. IRAS of CO on Rh/Fe₃O₄(001)

4.1. Three different CO species

To enable a direct comparison with the STM and DFT results summarised in Figure 1, IRAS measurements were performed on a Rh-decorated Fe₃O₄(001) sample with Rh coverages that had been previously characterised in detail.^{42,46} Figure 2 shows p-polarised IRAS spectra acquired after exposure to 3.4 langmuirs (L; 1 L = 1.33×10^{-6} mbar.s) of ¹³CO at room temperature for two different Rh coverages, 0.2 ML (black spectrum) and 0.4 ML (blue spectrum). In all experiments, the reference spectrum R_0 was recorded after Rh deposition but prior to CO dosing at 300 K, ensuring that only CO-induced changes appear in the spectra. For 0.2 ML Rh, three distinct absorption bands are observed in the CO-stretching region at 1979, 2037, and 2059 cm⁻¹. All three features are also present at 0.4 ML Rh and increase in intensity with increasing Rh coverage, indicating that each originates from CO adsorbed on Rh-related sites. The positions of the three bands remain nearly unchanged in the 0.4 ML spectrum, which suggests that dipole–dipole interactions between neighbouring CO molecules are negligible.

This is consistent with the previous STM studies,^{42,46} which show that the nearest-neighbour distance between Rh₁ adatoms on Fe₃O₄(001) is fixed by the surface reconstruction at 8.4 Å.

Based on the CO stretch frequencies calculated by DFT (Table 1), we assign the low-frequency peak at 1979 cm⁻¹ to CO adsorbed on the twofold coordinated Rh₁ sites (Fig. 1b). The relatively high intensity of this band is consistent with STM results, which show that Rh₁CO species are by far the most abundant configurations containing CO under these conditions.⁴⁶ We note, however, that IRAS peak intensities are not solely determined by the population of a given species, but also depend on the magnitude and orientation of the dynamic dipole moment relative to the surface normal, and on the detailed bonding geometry.

Table 1. Experimental and calculated C–O stretching frequencies, together with calculated CO adsorption energies for the different adsorption configurations. The calculated adsorption energies and frequencies are obtained from DFT calculations with and without Hubbard U correction applied to the Rh 4d states.

Configuration	E_{ads} , CO (eV)	$\tilde{\nu}_{\text{DFT},^{13}\text{CO}}$ (cm ⁻¹)		$\tilde{\nu}_{\text{exp},^{13}\text{CO}}$ (cm ⁻¹)	$\tilde{\nu}_{\text{DFT},^{12}\text{CO}}$ (cm ⁻¹)		$\tilde{\nu}_{\text{exp},^{12}\text{CO}}$ (cm ⁻¹)
		$U_{\text{eff, Rh}} = 0$	$U_{\text{eff, Rh}} = 3.61$ eV		$U_{\text{eff, Rh}} = 0$	$U_{\text{eff, Rh}} = 3.61$ eV	
Rh₁CO	-2.52	1971	1978	1979	2021	2029	2026
Rh₁(CO)₂	-2.37	2022 (sym)	2023 (sym)	2037	2076 (sym)	2076 (sym)	2085
		1961 (asym)	1974 (asym)		2012 (asym)	2025 (asym)	
Rh₅-foldCO	-2.19	2025	2047	2059	2078	2100	2106

The two higher-frequency bands at 2037 cm⁻¹ and 2059 cm⁻¹ appear with much lower intensity than the dominant 1979 cm⁻¹ band in both spectra. As mentioned previously, only small populations of Rh₂ dimers (the precursors of gem-dicarbonyls) and Rh₅-fold sites are present at this coverage. This low abundance is reflected in the correspondingly weak intensity of these two features. Based on DFT, the assignment of these two peaks is uncertain since the calculation without U on the Rh 4d states yields almost identical frequencies for the symmetric mode of the gem-dicarbonyl and the CO at the Rh₅-fold embedded in the surface. In the following, we will demonstrate that the assignment of the IR bands to the configurations in Figure 2 and Table 1 is correct, although the agreement between DFT and experiment is worse than for the Rh₁CO.

In principle, one could also consider whether one of the two high-frequency IRAS peaks originates from CO adsorbed on small Rh clusters. However, at a coverage <0.5 ML Rh, the amount of Rh clusters is negligible.³⁹ Moreover, because clusters exhibit a wide distribution of sizes and geometries, their vibrational signatures are typically broad rather than sharp, unlike the well-defined peaks observed in Fig. 2. Finally, CO adsorbed on small Rh clusters normally exhibits lower stretching frequencies (≈ 2040 cm⁻¹ for ¹²CO).⁶²

Table 1 shows that the CO stretch frequencies are directly correlated to the adsorption energies. A strong Rh-CO interaction is associated with back-donation from Rh 4d into the CO 2π* orbital, weakening the C–O bond and shifting its stretching frequency to lower values.^{63–66}

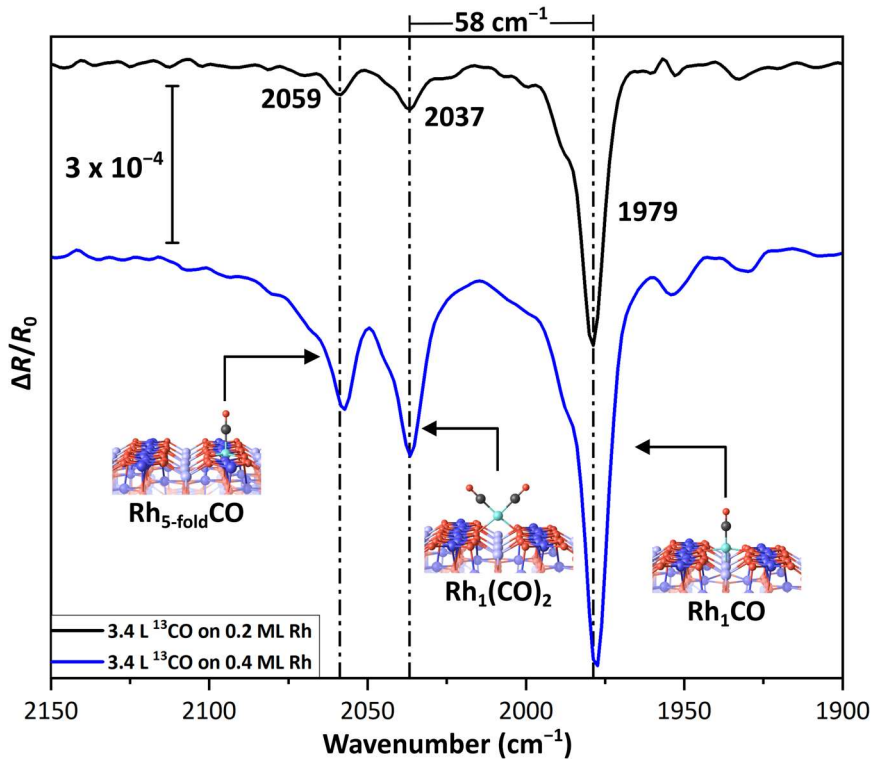


Figure 2. High-resolution IRAS spectra of ¹³CO adsorbed on Rh/Fe₃O₄(001). p-polarised IRAS spectra of Rh-decorated Fe₃O₄(001) with Rh coverages of 0.2 ML (black) and 0.4 ML (blue) after 3.4 L ¹³CO exposure. ¹³CO was introduced to the surface at room temperature, and the IRAS spectra were collected under identical conditions at $T = 300$ K. Three distinct vibrational bands are observed at 1979, 2037, and 2059 cm⁻¹, whose intensities increase with Rh coverage. These features are assigned to CO adsorbed on twofold coordinated Rh₁ sites, the symmetric stretch of gem-dicarbonyl Rh₁(CO)₂ species, and CO adsorbed on Rh_{5-fold} sites, respectively. Spectra were acquired with 4 cm⁻¹ resolution and averaged over 4000 scans (≈ 20 min acquisition time per spectrum).

4.2. Annealed Rh/Fe₃O₄(001): Increase of Rh_{5-fold} sites

As shown in previous STM and XPS studies^{39,42}, twofold Rh₁ adatoms are stable only below 400 K. Upon heating above this temperature, these species begin to incorporate into the surface lattice, forming fivefold and sixfold Rh sites. This structural transformation should be detectable by IRAS, as CO molecules adsorbed on twofold and fivefold Rh sites exhibit distinct

C–O stretching frequencies, whereas Rh_{6-fold} is below the surface and therefore not capable of CO adsorption. Figure 3 presents p-polarised IRAS spectra of Rh/Fe₃O₄(001) surfaces that all had the same initial Rh coverage of 0.2 ML but underwent different thermal treatments prior to 3.4 L ¹³CO dosing, leading to a different distribution of Rh species. The black spectrum corresponds to the as-deposited sample, which was kept at room temperature, and is identical to the one shown in Figure 2.

For the orange spectrum, the sample was briefly flashed to \approx 420 K after Rh deposition and then cooled back to 300 K. The spectrum shows a pronounced increase in the intensity of the high-frequency band at 2059 cm^{−1}, consistent with its assignment to monocarbonyls on Rh_{5-fold} sites that form upon thermal conversion of twofold Rh₁ species. The accompanying decrease in the low-frequency peak further supports this interpretation. The shoulder of the peak at 1979 cm^{−1} is attributed to CO adsorbed on twofold Rh₁ adatoms located at defect sites, primarily antiphase domain boundaries (APDBs) and sites above additional subsurface Fe_{oct} cations, as described in our previous studies^{67,68}. Such defect sites can also stabilise Rh₁ in a twofold coordination with a slightly higher adsorption energy, resulting in a weaker Rh–CO interaction and consequently a blue shift of the C–O stretching frequency. The shoulder appears more distinct in the orange spectrum mainly because the 1979 cm^{−1} peak undergoes a slight red shift after flashing to \approx 420 K. A similar small shift is observed for the intermediate band at 2037 cm^{−1}. These small shifts likely reflect subtle changes in the Rh–CO interaction strength due to modest modifications in the electronic structure of the surface and subsurface layers. Such changes can accompany structural rearrangements in which some twofold Rh₁ adatoms convert into fivefold surface species, while others incorporate into subsurface positions to form Rh_{6-fold}, as seen previously for Rh and other transition metal adatoms^{38,42}. The nearly unchanged intensity of the shoulder compared to the black spectrum indicates that regular twofold Rh₁ species are the first to convert into Rh_{5-fold}, while those associated with defects remain stable after this brief heat treatment.

The red spectrum in Figure 3 was recorded at 300 K after annealing the surface for 5 minutes at 420 K. This longer temperature treatment further decreases the intensity of both the low-frequency Rh₁CO band and its shoulder, while the high-frequency band assigned to CO on Rh_{5-fold} becomes more intense. This provides direct experimental support for the peak assignments, as it is consistent with earlier STM and XPS observations of the evolution of Rh species under comparable annealing conditions.^{39,42} In contrast to the behaviour of the twofold band, the fivefold band shows a slight blue shift after annealing, likely reflecting a modest reduction in π -backdonation from Rh_{5-fold} to CO as they become more tightly integrated into the surface lattice. The resulting weaker Rh–CO bond leads to a slightly higher C–O stretching frequency, in agreement with the observed shift.

Although the shift in intensity from the low- to the high-frequency band provides clear qualitative evidence for their assignment to CO on twofold and fivefold Rh sites, respectively, it remains difficult to determine quantitatively how many twofold Rh₁ atoms convert into Rh_{5-fold} upon annealing. This is because CO binds in different geometries on the two sites, leading to different orientations of the vibrational dipole moment relative to the surface, and, possibly,

different magnitudes of the dipole moment. CO adsorbed on Rh₅-fold stands upright, so its dipole moment change is normal to the surface and couples strongly to the perpendicular component of p-polarised light. In contrast, CO bound to twofold Rh₁ adopts a pseudo-square-planar geometry and is tilted, resulting in both perpendicular and in-plane components of the dipole moment. Our measurements were conducted with p-polarised light at non-grazing incidence angles below 74°. At these incidence angles, perpendicular dipoles produce strong negative features, whereas in-plane dipoles give much weaker positive signals (approximately one-fifteenth of the perpendicular intensity if the dipole is parallel to the incidence plane, and no signal in p polarisation for the case of a dipole moment normal to the incidence plane; see Figure S1). Consequently, the intensities of the two peaks are not a quantitative measure of the abundance of these species.

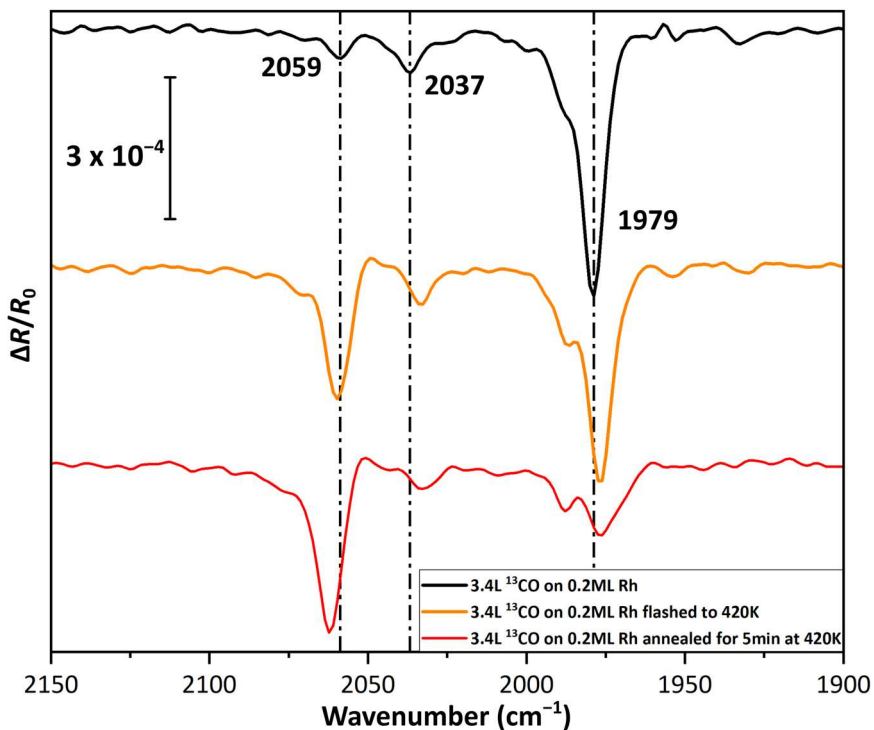


Figure 3. Thermally induced conversion of twofold to fivefold Rh sites monitored by IRAS: p-polarised IRAS spectra of Rh-decorated Fe₃O₄(001) surfaces (initial Rh coverage 0.2 ML) subjected to different thermal treatments prior to 3.4 L ¹³CO exposure. The black spectrum corresponds to the as-deposited sample kept at 300 K (same as Figure 2). The orange spectrum was obtained after a brief flash to 420 K followed by cooling to 300 K, while the red spectrum was recorded after annealing the surface for 5 min at 420 K. All spectra were measured at 300 K after CO exposure.

4.3. Isotopic confirmation of the gem-dicarbonyl band

To provide direct experimental confirmation of the assignment of the mid-frequency peak to gem-dicarbonyl Rh₁(CO)₂ species, isotopic substitution experiments were performed using

^{12}CO , ^{13}CO , and an equimolar $^{12}\text{CO}/^{13}\text{CO}$ mixture on identically prepared 0.4 ML Rh/Fe₃O₄(001) surfaces. Figure 4 presents the corresponding p-polarised IRAS spectra. The top (blue) spectrum corresponds to ^{13}CO , identical to that shown in Figure 2; the bottom (purple) to ^{12}CO ; and the middle (dark violet) to the $^{12}\text{CO}/^{13}\text{CO}$ mixture.

As expected, the pure ^{12}CO and ^{13}CO spectra each display three absorption bands of comparable relative intensity, with all ^{13}CO features shifted to lower frequencies by $\approx 47\text{ cm}^{-1}$ relative to the other isotope. This isotopic shift is consistent with the change in the reduced mass of the C–O bond and is in excellent agreement with the harmonic-oscillator model. For monocarbonyl species adsorbed on Rh atoms, exposure to an equimolar mixture of ^{12}CO and ^{13}CO should yield two peaks of similar intensity separated by $\approx 47\text{ cm}^{-1}$, corresponding to identical Rh sites bonded to either isotope. This behaviour is indeed observed in the mixed-isotope (dark violet) spectrum for the two peaks at 1979 and 2059 cm^{-1} with ^{13}CO (2106 and 2026 cm^{-1} with ^{12}CO), confirming their assignment as monocarbonyl Rh–CO species. In contrast, gem-dicarbonyls behave differently: co-adsorption of ^{12}CO and ^{13}CO should produce a third, intermediate band between the pure-isotope peaks, arising from mixed-isotope $\text{Rh}_1(^{12}\text{CO})(^{13}\text{CO})$ species. The appearance of such an intermediate band is a well-established fingerprint of intramolecular vibrational coupling between the two CO ligands, as reported previously by Frank *et al.*²⁶

In the present case, the mixed-isotope spectrum reveals a new feature at 2068 cm^{-1} , providing solid evidence that the mid-frequency band in the pure-isotope spectra originates from $\text{Rh}_1(\text{CO})_2$ rather than from distinct monocarbonyl species. The measured peak separations between the symmetric ^{12}CO and mixed-isotope bands ($\approx 17\text{ cm}^{-1}$), and between the mixed-isotope and ^{13}CO bands ($\approx 31\text{ cm}^{-1}$), are fully consistent with the previously reported coupling strengths for gem-dicarbonyls on Rh atoms supported on NiAl(110).²⁶ Furthermore, the approximately two-fold higher intensity of the mixed-isotope 2068 cm^{-1} band relative

to the pure ^{13}CO dicarbonyl feature is fully consistent with statistical expectations: in an equimolar $^{12}\text{CO}/^{13}\text{CO}$ mixture, the probability of forming $\text{Rh}_1(^{13}\text{CO})(^{12}\text{CO})$ is twice that of forming $\text{Rh}_1(^{13}\text{CO})_2$ or $\text{Rh}_1(^{12}\text{CO})_2$.

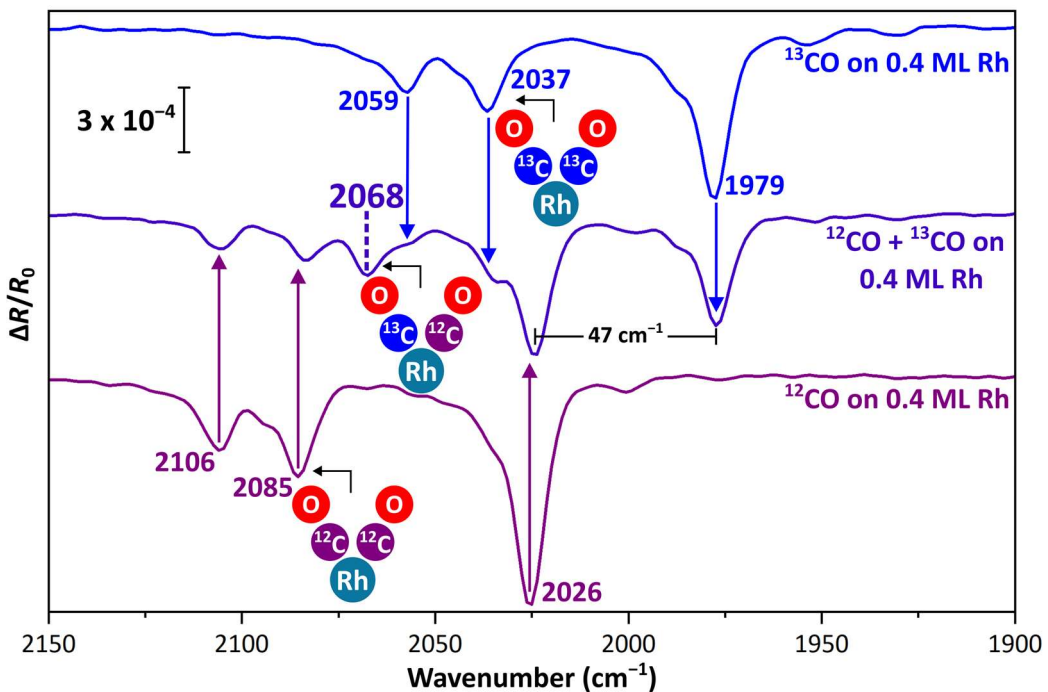


Figure 4. Isotopic confirmation of the gem-dicarbonyl assignment. p-polarized IRAS spectra recorded at 300 K after exposing 0.4 ML Rh/Fe₃O₄(001) to ¹³CO (blue), ¹²CO (purple), and an equimolar ¹²CO/¹³CO mixture (dark violet). Each pure-isotope spectrum exhibits three bands corresponding to CO adsorbed on twofold and fivefold Rh sites, as well as the symmetric stretch of the Rh₁(CO)₂ gem-dicarbonyl. In the ¹²CO spectrum, all ¹³CO features are shifted to lower frequency by $\approx 47 \text{ cm}^{-1}$, consistent with the expected isotopic dependence of the C–O stretching mode. In the mixed-isotope experiment, an additional intermediate band appears between the pure-¹²CO and pure-¹³CO gem-dicarbonyl peaks, arising from vibrational coupling within mixed-isotope Rh₁(¹³CO)(¹²CO) species at 2068 cm⁻¹, see sketch. The presence of this intermediate feature provides unambiguous evidence that the mid-frequency band at $\approx 2037 \text{ cm}^{-1}$ (for ¹³CO) originates from a gem-dicarbonyl species rather than a monocarbonyl. The relative intensities of the three gem-dicarbonyl peaks in the mixed-isotope spectrum are consistent with the expected 1:2:1 statistical distribution for an equimolar ¹²CO/¹³CO mixture.

Gem-dicarbonyls exhibit two characteristic C–O stretching modes, a symmetric and an asymmetric stretch,^{18,22,27,69,70} but we have only discussed the symmetric stretch so far. In powder catalysts, both bands appear as minima in relative reflectivity (i.e., upward absorbance peaks) because the crystallites are randomly oriented with respect to the incident IR light. On a single-crystal surface, the sign and magnitude of $\Delta R/R_0$ depend on dipole orientation, light polarisation, and incidence angle, as described by the Fresnel equations (Figure S1). Perpendicular dipole components give strong negative bands, whereas in-plane dipoles generate much weaker positive features. The symmetric stretch of the Rh₁(CO)₂ gem-dicarbonyl has a net dipole-moment change normal to the surface and therefore appears as the negative peak (2037 cm⁻¹ for ¹³CO). In contrast, the asymmetric stretch exhibits an in-plane dipole moment change and would appear as a very weak, positive band. In a recent IRAS study of Rh gem-dicarbonyls on TiO₂(110), Eder *et al.*⁶² observed the asymmetric stretch as a weak positive peak

$\approx 61\text{ cm}^{-1}$ below the symmetric stretch peak, in excellent agreement with DFT predictions. Thus, in our spectra, the asymmetric stretch would be extremely weak compared with the symmetric stretch at 2037 cm^{-1} and would fall below the noise level. Moreover, its expected frequency coincides almost exactly with the intense Rh_1CO monocarbonyl band at 1979 cm^{-1} , which lies 58 cm^{-1} below the symmetric stretch—very close to the offset reported by Eder *et al.*⁶² and to values known from powder catalysts.^{22,69,70}

The 0.4 ML spectrum in Figure 2 shows that the relative intensities of both the high-frequency band at 2059 cm^{-1} and the intermediate band at 2037 cm^{-1} increase more strongly with Rh Coverages than that of the dominant twofold Rh_1CO band (See Table S1). This behaviour is fully consistent with our peak assignment. For the Rh_5 -fold embedded in the surface, it has been shown that its occurrence markedly increases with an increase of the Rh coverage to 0.5 ML.³⁹ Likewise, Rh_2 dimers become more abundant at higher Rh coverages because they are $\approx 0.19\text{ eV}$ more stable than isolated Rh_1 adatoms,⁴⁶ which leads to a higher concentration of $\text{Rh}_1(\text{CO})_2$ gem-dicarbonyls upon CO exposure under UHV conditions. To determine whether gem-dicarbonyls remain a minority species also at elevated pressures, we carried out complementary near-ambient-pressure STM measurements, which are presented in the next section.

5. Near-ambient-pressure STM: sequential CO adsorption at elevated pressure

As described in section 3, in UHV experiments, dicarbonyls can form only via dissociation of Rh_2 dimers.⁴⁶ To test whether this restriction persists at higher pressures, we examined CO adsorption on $\text{Rh}/\text{Fe}_3\text{O}_4(001)$ using NAP-STM. After standard UHV preparation and a brief low-dose CO exposure ($\approx 3\text{ L}$), STM imaging confirmed that the surface contained primarily monocarbonyl Rh_1CO species, as in all previous UHV studies. When a much higher CO dose was applied, 2 mbar for 3 min at room temperature, the surface changed dramatically. STM images recorded at 2 mbar CO [Fig. 5(a)] showed that essentially all Rh_1CO species adopt a double-lobed geometry identical to the $\text{Rh}_1(\text{CO})_2$ gem-dicarbonyls observed in UHV only after CO-induced dissociation of Rh_2 dimers [red arrow in Fig. 5(a)]. Under these near-ambient conditions, however, the gem-dicarbonyls appear in the absence of any monocarbonyl neighbours (which would result from the Rh-dimer mediated mechanism of dicarbonyl formation), demonstrating that the dicarbonyls now form directly from isolated Rh_1CO monocarbonyls. These gem-dicarbonyls were also observed after dosing was stopped and the chamber pumped to UHV conditions, in agreement with the stability of dicarbonyl species inferred from the adsorption energy (Fig. S2). A blank experiment on clean $\text{Fe}_3\text{O}_4(001)$ showed no adsorption, confirming that the species observed originate from Rh.

These findings directly validate the kinetic interpretation from our earlier STM/DFT work.⁴⁶ In that study, we showed that sequential adsorption of a second CO molecule on Rh_1CO requires a metastable precursor configuration approximately 0.5 eV above the ground state [Fig. 5(b)], corresponding to a configurational probability on the order of 10^{-8} or 10^{-9} at 300 K. In UHV, where CO is typically dosed in the 10^{-8} mbar range, the collision rate at each Rh_1 site is only on the order of 10^{-2} to 10^{-3} s^{-1} (one CO impact every few hundreds of seconds), so the effective

rate for an additional CO impacting a monocarbonyl while it is in its rare precursor geometry is essentially zero on experimental timescales. Based on TPD results,⁷¹ we estimate that the residence time of a CO molecule on the Fe₃O₄(001) surface at RT is in the nanosecond regime; thus the CO can diffuse and visit one or a few Rh₁CO monocarbonyls before desorbing. This means that precursor-mediated adsorption should be possible, and the actual reaction rate might be up to ≈ 3 orders of magnitude higher than the estimate based on direct impingement of CO on the Rh₁CO. Nevertheless, the rate of Rh₁(CO)₂ formation via CO attachment to Rh₁CO remains negligible in a UHV experiment.

At millibar pressures, the situation is completely different: at 2 mbar, the same site experiences roughly 10⁶ direct CO collisions per second, so even configurations with probabilities near 10⁻⁹ are sampled frequently enough for the sequential adsorption pathway to create the dicarbonyl within much less than an hour. Assuming the precursor mechanism discussed above, the timescale of Rh₁(CO)₂ formation might be in the range of a few seconds. Under these conditions, direct formation of Rh₁(CO)₂ becomes viable, fully consistent with the NAP-STM observations.

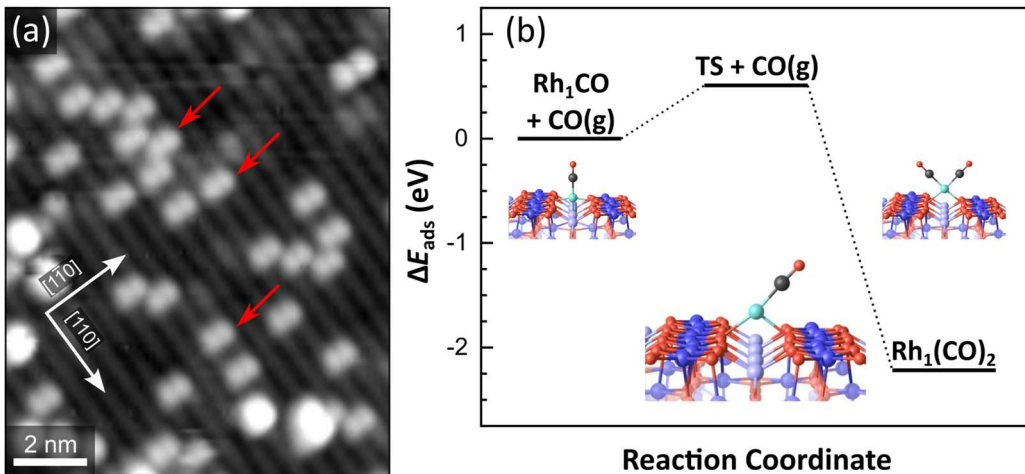


Figure 5: Exposure of Rh/Fe₃O₄(001) to 2 mbar CO. (a) NAP-STM image ($V_{\text{sample}} = 2.2$ V; $I = 0.02$ nA) of 0.2 ML Rh/Fe₃O₄(001) under 2 mbar CO. Two-lobe features are observed as the dominant species and are assigned to gem-dicarbonyls formed by adsorption of a second CO molecule on Rh₁CO species (red arrows in Fig. 1a). (b) Adsorption of a second CO molecule onto the monocarbonyl configuration proceeds via a metastable transition state (TS), occupied $\approx 10^{-8}$ or 10^{-9} of the time at room temperature, as deduced from DFT calculations in our previous study.⁴⁶ Energies are given relative to the monocarbonyl ground state.

5. Discussion

The results presented here demonstrate that IRAS experiments on single crystals under well-defined conditions can provide quantitatively reliable, site-resolved vibrational fingerprints for oxide-supported single-atom catalysts. Using Rh/Fe₃O₄(001) as an exemplary model system, we resolve three distinct Rh–CO species, namely monocarbonyls, and gem-dicarbonyls of twofold coordinated Rh₁ adatoms, as well as monocarbonyls formed at fivefold-coordinated Rh atoms embedded in the surface. We could assign the vibrational frequencies v_{CO} unambiguously

to these species by combining isotope substitution, annealing experiments, STM/nc-AFM imaging, XPS, TPD, and DFT-based calculations. The coordination-dependent shifts in ν_{CO} provide a direct handle on the local environment of Rh and can be used as a reference when analysing the more complex CO-IR spectra of supported Rh powder catalysts.^{18,24,25,28,69,70}

The present study also clarifies how single-crystal IRAS relates to CO-IR spectra on powders. On powder catalysts, randomly oriented crystallites and averaging over all incidence angles mean that both symmetric and asymmetric gem-dicarbonyl stretches typically appear as bands of increased absorption.^{18,24,25,28,69,70} On the single-crystal Rh/Fe₃O₄(001) model system, by contrast, the fixed surface orientation and chosen incidence angle range make the IRAS intensity strongly dependent on dipole direction: components normal to the surface dominate, while in-plane components contribute only weak, oppositely signed features. This explains why we only observe the symmetric stretch of the gem-dicarbonyl and do not observe the asymmetric mode, even though both are prominent in powder spectra. While the spectra therefore differ in the intensities of the IR bands, the fingerprint positions of the IR-active species remain unaffected, making UHV-based IRAS studies valuable for identifying, assigning and benchmarking surface species.

The comparison with theory highlights both the strengths and limitations of current DFT approaches. DFT+U calculations correctly predict the relative ordering of ν_{CO} for the Rh₁CO and Rh₁(CO)₂ species at 2-fold coordinated Rh₁ adatom sites, and the calculated adsorption energies rule out gem-dicarbonyl formation at Rh₅-fold sites. On the other hand, the calculated difference between the symmetric stretch of Rh₁(CO)₂ and the CO stretch frequency at Rh₅-fold strongly depends on details of the computational approach (whether a Hubbard U is used for the Rh), so assigning these bands purely on the basis of the calculated frequencies would be ambiguous. Since the CO frequency depends on the charge of the Rh,⁶⁶ we attribute this sensitivity to the different charge states of Rh at these sites: At twofold sites, Rh₁ is singly charged⁴⁶, while the calculated Bader charge of the Rh₅-fold is 1.27 e (1.23 e with $U_{\text{eff},\text{Rh}} = 3.61$ eV), indicating a Rh²⁺ or Rh³⁺ state. Usually, the Rh³⁺ oxidation state is more common, but less likely to form stable carbonyls than Rh²⁺.⁶⁶ In our calculations, the Hubbard U mainly shifts the ν_{CO} on the Rh₅-fold, while the other configurations are much less affected. Employing U is common for similar systems with 3d transition elements,⁴⁷ but it is often neglected for the 4d and 5d metals since several works indicate that U values for 4d elements are lower and therefore of less importance.^{72,73} Other work, however, indicates similar U values for Fe and Rh.⁷⁴ Given that, in the present system, using $U_{\text{eff},\text{Rh}} = 3.61$ eV significantly improves the agreement between calculated and experimental ν_{CO} at Rh₅-fold, it may be worthwhile to re-examine the role of Hubbard corrections for 4d (and possibly 5d) elements more generally, even though a single case study is clearly insufficient to justify a universal prescription.

Since the configuration corresponding to each frequency can be unambiguously determined by our experiments, the experimental spectra provide a valuable benchmark for refining

computational treatment of metal–CO bonding on oxides. More broadly, the combination of well-defined model surfaces, high-quality IRAS, and complementary microscopy across the UHV–near-ambient range offers a general strategy for understanding the CO-IR signatures of isolated metal sites in real catalysts. This allows identification of which structural motifs and formation pathways are actually relevant under working conditions.

A central mechanistic insight concerns the formation of gem-dicarbonyls. Under UHV, gem-dicarbonyl $\text{Rh}_1(\text{CO})_2$ species arise almost exclusively from CO-induced dissociation of Rh_2 dimers, even though the formation of a dicarbonyl from a monocarbonyl is thermodynamically favourable. This behaviour reflects a strong kinetic constraint: sequential adsorption of a second CO molecule onto a monocarbonyl requires a metastable precursor geometry with very low configurational probability, which cannot be accessed at the low collision rates present during UHV dosing. As shown by the NAP-STM experiments in Section 5, this restriction is lifted at millibar CO pressures, where gem-dicarbonyls form directly on isolated Rh_1 sites and dominate the surface coverage. The combination of UHV and NAP thus provides a coherent picture in which UHV acts as a kinetic filter that isolates individual reaction channels, while near-ambient measurements reveal which pathways dominate under closer conditions to applied catalysis.

Conclusions

The results demonstrate how IRAS can serve as a bridging technique between idealised model systems and applied systems under realistic conditions. Using $\text{Rh}/\text{Fe}_3\text{O}_4(001)$ as a model system in UHV, we resolved and assigned the key Rh carbonyl species present on the surface: monocarbonyls and gem-dicarbonyls at twofold Rh_1 sites, as well as monocarbonyls formed by fivefold coordinated Rh embedded in the surface. Under UHV conditions, gem-dicarbonyls are a minority species since they form almost exclusively via CO-induced dissociation of Rh_2 dimers, because the sequential adsorption of two CO molecules on an isolated Rh_1 is kinetically blocked despite being thermodynamically favoured. Near-ambient-pressure STM shows that at millibar CO pressures this kinetic limitation is lifted and gem-dicarbonyls form directly on isolated Rh_1 sites, reconciling UHV model studies with the gem-dicarbonyl signatures commonly observed under catalytic conditions. The experimental CO stretch frequencies are valuable as fingerprints for oxide-supported single-atom catalysts. Comparison with DFT+U highlights that theory does not yet match experimental frequencies quantitatively, underlining the value of the IRAS benchmarks established here for interpreting CO-IR spectra and refining theoretical descriptions of metal–CO bonding on oxide-supported single-atom catalysts.

Data availability

The data supporting this article have been included as part of the Supplementary Information.

Author contributions

NEHB contributed to the investigation, performed formal analysis, data curation, visualisation, and prepared the original draft. CW assisted with data analysis and investigation. PS carried out the theoretical and methodological work, contributed to formal analysis and visualisation. DR supported methodology and contributed to experimental investigation. AL, FL, MO, and LP

performed experimental investigation. ZJ contributed to investigation and formal analysis. FK performed data analysis and visualisation. ME contributed to methodology. MS, UD, MM, and CF contributed to the methodology and validation. PM contributed to investigation and methodology. JP contributed to conceptualisation, supervision, validation, and funding acquisition. GSP contributed to conceptualisation, supervision, validation, funding acquisition, and writing of the original draft. All authors participated in reviewing & editing of the manuscript.

Conflicts of interest

There are no conflicts to declare.

Acknowledgements

Funding from the European Research Council (ERC) under the European Union's Horizon 2020 research and innovation programme (grant agreement No. [864628], Consolidator Research Grant 'E-SAC') is acknowledged. This research was funded in part by the Austrian Science Fund (FWF) 10.55776/F81 and the Cluster of Excellence MECS (10.55776/COE5). Jiri Pavelec and Adam Lagin gratefully acknowledge financial support from the FWF through project number 10.55776/I6732. Chunlei Wang gratefully acknowledges financial support from the FWF through project number 10.55776/PAT1934924. Matthias Meier gratefully acknowledges financial support from the FWF through project number 10.55776/PAT2176923. Moritz Eder acknowledges funding by the Marie Skłodowska-Curie Actions (Project 101103731, SCI-PHI). The authors acknowledge the CERIC-ERIC consortium (proposal ID 20252185) for access to experimental facilities and financial support. Peter Matvija acknowledges the financial support from the Ministry of Education, Youth, and Sports of the Czech Republic under project LM2023072. The Austrian Scientific Computing was used to obtain the computational results. For open access purposes, the authors have applied a CC BY public copyright license to any author-accepted manuscript version arising from this submission.

Notes and references

- a. Institute of Applied Physics, TU Wien, 1040 Vienna, Austria
- b. Department of Surface and Plasma Science, Charles University in Prague, V Holesovickach 2, 180 00 Praha, Czech Republic
- c. Central European Institute of Technology (CEITEC), Brno University of Technology, Brno, 612 00, Czechia
- d. Faculty of Physics and Center for Computational Materials Science, University of Vienna, Vienna AT 1090, Austria
- e. Dipartimento di Fisica e Astronomia, Università di Bologna, Bologna IT 40126, Italy

* jiri.pavelec@tuwien.ac.at

1 F. Zaera, In-situ and operando spectroscopies for the characterization of catalysts and of mechanisms of catalytic reactions, *J. Catal.*, 2021, **404**, 900–910.

2 F. C. Meunier, Pitfalls and benefits of in situ and operando diffuse reflectance FT-IR spectroscopy (DRIFTS) applied to catalytic reactions, *React. Chem. Eng.*, 2016, **1**, 134–141.

3 E. Groppo, S. Rojas-Buzo and S. Bordiga, The Role of *In Situ / Operando* IR Spectroscopy in Unraveling Adsorbate-Induced Structural Changes in Heterogeneous Catalysis, *Chem. Rev.*, 2023, **123**, 12135–12169.

4 K. Zhao, J. Zhang, W. Luo, M. Li, E. Moioli, M. Spodaryk and A. Züttel, A combined diffuse reflectance infrared Fourier transform spectroscopy–mass spectroscopy–gas chromatography for the *operando* study of the heterogeneously catalyzed CO₂ hydrogenation over transition metal-based catalysts, *Rev. Sci. Instrum.*, 2020, **91**, 074102.

5 C. Rodríguez, S. Moreno and R. Molina, Operando DRIFT-MS study of oxidative steam reforming of ethanol (OSRE) on Ni-Co mixed oxides under non-equilibrium conditions, *Chem. Eng. J.*, 2024, **480**, 148243.

6 J. Ryczkowski, IR spectroscopy in catalysis, *Catal. Today*, 2001, **68**, 263–381.

7 L. Liu and A. Corma, Metal Catalysts for Heterogeneous Catalysis: From Single Atoms to Nanoclusters and Nanoparticles, *Chem. Rev.*, 2018, **118**, 4981–5079.

8 M. Carosso, T. Fovanna, A. Ricchebuono, E. Vottero, M. Manzoli, S. Morandi, R. Pellegrini, A. Piovano, D. Ferri and E. Groppo, Gas phase vs. liquid phase: monitoring H₂ and CO adsorption phenomena on Pt/Al₂O₃ by IR spectroscopy, *Catal. Sci. Technol.*, 2022, **12**, 1359–1367.

9 I. Jbir, A. Paredes-Nunez, S. Khaddar-Zine, Z. Ksibir, F. Meunier and D. Bianchi, Heat of adsorption of CO on EUROPT-1 using the AEIR method: Effect of analysis parameters, water and sample mode, *Appl. Catal. Gen.*, 2015, **505**, 309–318.

10 T. Elgayyar, R. Atwi, A. Tuel and F. C. Meunier, Contributions and limitations of IR spectroscopy of CO adsorption to the characterization of bimetallic and nanoalloy catalysts, *Catal. Today*, 2021, **373**, 59–68.

11 S. K. Cheah, V. P. Bernardet, A. A. Franco, O. Lemaire and P. Gelin, Study of CO and Hydrogen Interactions on Carbon-Supported Pt Nanoparticles by Quadrupole Mass Spectrometry and Operando Diffuse Reflectance FTIR Spectroscopy, *J. Phys. Chem. C*, 2013, **117**, 22756–22767.

12 L. DeRita, S. Dai, K. Lopez-Zepeda, N. Pham, G. W. Graham, X. Pan and P. Christopher, Catalyst Architecture for Stable Single Atom Dispersion Enables Site-Specific Spectroscopic and Reactivity Measurements of CO Adsorbed to Pt Atoms, Oxidized Pt Clusters, and Metallic Pt Clusters on TiO₂, *J. Am. Chem. Soc.*, 2017, **139**, 14150–14165.

13 L. DeRita, J. Resasco, S. Dai, A. Boubnov, H. V. Thang, A. S. Hoffman, I. Ro, G. W. Graham, S. R. Bare, G. Pacchioni, X. Pan and P. Christopher, Structural evolution of atomically dispersed Pt catalysts dictates reactivity, *Nat. Mater.*, 2019, **18**, 746–751.

14 M. J. Kale and P. Christopher, Utilizing Quantitative *in Situ* FTIR Spectroscopy To Identify Well-Coordinated Pt Atoms as the Active Site for CO Oxidation on Al_2O_3 -Supported Pt Catalysts, *ACS Catal.*, 2016, **6**, 5599–5609.

15 S. H. Oh and J. E. Carpenter, The oxidation state and catalytic activity of supported rhodium, *J. Catal.*, 1983, **80**, 472–478.

16 H. Tanaka, M. Taniguchi, M. Uenishi, N. Kajita, I. Tan, Y. Nishihata, J. Mizuki, K. Narita, M. Kimura and K. Kaneko, Self-Regenerating Rh- and Pt-Based Perovskite Catalysts for Automotive-Emissions Control, *Angew. Chem. Int. Ed.*, 2006, **45**, 5998–6002.

17 H. Asakura, S. Hosokawa, T. Ina, K. Kato, K. Nitta, K. Uera, T. Uruga, H. Miura, T. Shishido, J. Ohyama, A. Satsuma, K. Sato, A. Yamamoto, S. Hinokuma, H. Yoshida, M. Machida, S. Yamazoe, T. Tsukuda, K. Teramura and T. Tanaka, Dynamic Behavior of Rh Species in Rh/ Al_2O_3 Model Catalyst during Three-Way Catalytic Reaction: An Operando X-ray Absorption Spectroscopy Study, *J. Am. Chem. Soc.*, 2018, **140**, 176–184.

18 A. J. Hoffman, C. Asokan, N. Gadias, E. Schroeder, G. Zakem, S. V. Nystrom, A. “Bean” Getsoian, P. Christopher and D. Hibbitts, Experimental and Theoretical Characterization of Rh Single Atoms Supported on $\gamma\text{-Al}_2\text{O}_3$ with Varying Hydroxyl Contents during NO Reduction by CO, *ACS Catal.*, 2022, **12**, 11697–11715.

19 K. E. Kartavova, M. Yu. Mashkin, M. Yu. Kostin, E. D. Finashina, K. B. Kalmykov, G. I. Kapustin, P. V. Pribytkov, O. P. Tkachenko, I. V. Mishin, L. M. Kustov and A. L. Kustov, Rhodium-Based Catalysts: An Impact of the Support Nature on the Catalytic Cyclohexane Ring Opening, *Nanomaterials*, 2023, **13**, 936.

20 C. Yang and C. W. Garl, Infrared Studies of Carbon Monoxide Chemisorbed on Rhodium, *J. Phys. Chem.*, 1957, **61**, 1504–1512.

21 J. A. Anderson and C. H. Rochester, Infrared study of CO adsorption on Pt–Rh/ Al_2O_3 catalysts, *J Chem Soc Faraday Trans*, 1991, **87**, 1479–1483.

22 G. Kim, S. Choung, J. Hwang, Y. Choi, S. Kim, D. Shin, J. W. Han and H. Lee, Highly Durable Rh Single Atom Catalyst Modulated by Surface Defects on Fe-Ce Oxide Solid Solution, *Angew. Chem. Int. Ed.*, 2025, **64**, e202421218.

23 S. Trautmann and M. Baerns, Infrared Spectroscopic Studies of CO Adsorption on Rhodium Supported by SiO_2 , Al_2O_3 , and TiO_2 , *J. Catal.*, 1994, **150**, 335–344.

24 A. B. Kroner, M. A. Newton, M. Tromp, O. M. Roscioni, A. E. Russell, A. J. Dent, C. Prestipino and J. Evans, Time-Resolved, *In Situ* DRIFTS/EDE/MS Studies on Alumina-Supported Rhodium Catalysts: Effects of Ceriation and Zirconiation on Rhodium–CO Interactions, *ChemPhysChem*, 2014, **15**, 3049–3059.

25 N. Yang and S. F. Bent, Investigation of inherent differences between oxide supports in heterogeneous catalysis in the absence of structural variations, *J. Catal.*, 2017, **351**, 49–58.

26 M. Frank, R. Kühnemuth, M. Bäumer and H.-J. Freund, Vibrational spectroscopy of CO adsorbed on supported ultra-small transition metal particles and single metal atoms, *Surf. Sci.*, 2000, **454–456**, 968–973.

27 E. K. Schroeder, J. Finzel and P. Christopher, Photolysis of Atomically Dispersed Rh/Al₂O₃ Catalysts: Controlling CO Coverage *in Situ* and Promoting Reaction Rates, *J. Phys. Chem. C*, 2022, **126**, 18292–18305.

28 S. Zhang, Y. Tang, L. Nguyen, Y.-F. Zhao, Z. Wu, T.-W. Goh, J. J. Liu, Y. Li, T. Zhu, W. Huang, A. I. Frenkel, J. Li and F. F. Tao, Catalysis on Singly Dispersed Rh Atoms Anchored on an Inert Support, *ACS Catal.*, 2018, **8**, 110–121.

29 F. C. Meunier, Relevance of IR Spectroscopy of Adsorbed CO for the Characterization of Heterogeneous Catalysts Containing Isolated Atoms, *J. Phys. Chem. C*, 2021, **125**, 21810–21823.

30 J. A. Mielczarski, External reflection infrared spectroscopy at metallic, semiconductor, and nonmetallic substrates. 1. Monolayer films, *J. Phys. Chem.*, 1993, **97**, 2649–2663.

31 M. Kira and S. W. Koch, Many-body correlations and excitonic effects in semiconductor spectroscopy, *Prog. Quantum Electron.*, 2006, **30**, 155–296.

32 J. Libuda, I. Meusel, J. Hoffmann, J. Hartmann, L. Piccolo, C. R. Henry and H.-J. Freund, The CO oxidation kinetics on supported Pd model catalysts: A molecular beam/ *in situ* time-resolved infrared reflection absorption spectroscopy study, *J. Chem. Phys.*, 2001, **114**, 4669–4684.

33 M. Sterrer, T. Risse and H.-J. Freund, Low temperature infrared spectra of CO adsorbed on the surface of MgO(001) thin films, *Surf. Sci.*, 2005, **596**, 222–228.

34 I. V. Yudanov, R. Sahnoun, K. M. Neyman, N. Rösch, J. Hoffmann, S. Schauermann, V. Johánek, H. Unterhalt, G. Rupprechter, J. Libuda and H.-J. Freund, CO Adsorption on Pd Nanoparticles: Density Functional and Vibrational Spectroscopy Studies, *J. Phys. Chem. B*, 2003, **107**, 255–264.

35 F. M. Hoffmann and M. D. Weisel, Fourier transform infrared reflection absorption spectroscopy studies of adsorbates and surface reactions: Bridging the pressure gap between surface science and catalysis, *J. Vac. Sci. Technol. Vac. Surf. Films*, 1993, **11**, 1957–1963.

36 G. Rupprechter, Sum Frequency Generation and Polarization–Modulation Infrared Reflection Absorption Spectroscopy of Functioning Model Catalysts from Ultrahigh Vacuum to Ambient Pressure, in *Advances in Catalysis*, Elsevier, 2007, vol. 51, pp. 133–263.

37 R. Bliem, E. McDermott, P. Ferstl, M. Setvin, O. Gamba, J. Pavelec, M. A. Schneider, M. Schmid, U. Diebold, P. Blaha, L. Hammer and G. S. Parkinson, Subsurface cation vacancy stabilization of the magnetite (001) surface, *Science*, 2014, **346**, 1215–1218.

38 R. Bliem, J. Pavelec, O. Gamba, E. McDermott, Z. Wang, S. Gerhold, M. Wagner, J. Osiecki, K. Schulte, M. Schmid, P. Blaha, U. Diebold and G. S. Parkinson, Adsorption and

incorporation of transition metals at the magnetite $\text{Fe}_3\text{O}_4(001)$ surface, *Phys. Rev. B*, 2015, **92**, 075440.

39 M. A. Sharp, C. J. Lee, M. Mahapatra, R. S. Smith, B. D. Kay and Z. Dohnálek, Preparation and Characterization of Model Homotopic Catalysts: Rh Adatoms, Nanoparticles, and Mixed Oxide Surfaces on $\text{Fe}_3\text{O}_4(001)$, *J. Phys. Chem. C*, 2022, **126**, 14448–14459.

40 Z. Jakub, J. Hulva, M. Meier, R. Bliem, F. Kraushofer, M. Setvin, M. Schmid, U. Diebold, C. Franchini and G. S. Parkinson, Local Structure and Coordination Define Adsorption in a Model $\text{Ir}_1/\text{Fe}_3\text{O}_4$ Single-Atom Catalyst, *Angew. Chem. Int. Ed.*, 2019, **58**, 13961–13968.

41 Z. Jakub, J. Hulva, F. Mirabella, F. Kraushofer, M. Meier, R. Bliem, U. Diebold and G. S. Parkinson, Nickel Doping Enhances the Reactivity of $\text{Fe}_3\text{O}_4(001)$ to Water, *J. Phys. Chem. C*, 2019, **123**, 15038–15045.

42 Z. Jakub, J. Hulva, P. T. P. Ryan, D. A. Duncan, D. J. Payne, R. Bliem, M. Ulreich, P. Hofegger, F. Kraushofer, M. Meier, M. Schmid, U. Diebold and G. S. Parkinson, Adsorbate-induced structural evolution changes the mechanism of CO oxidation on a Rh/ Fe_3O_4 (001) model catalyst, *Nanoscale*, 2020, **12**, 5866–5875.

43 C. J. Lee, M. A. Sharp, B. A. Jackson, M. Mahapatra, S. Raugei, L. Árnadóttir, M.-S. Lee, B. D. Kay and Z. Dohnálek, Dynamic Activation of Single-Atom Catalysts by Reaction Intermediates: Conversion of Formic Acid on Rh/ $\text{Fe}_3\text{O}_4(001)$, *ACS Catal.*, 2024, **14**, 15396–15406.

44 M. Mahapatra, M. A. Sharp, C. J. Lee, Y. Zhu, O. Y. Gutiérrez, B. D. Kay and Z. Dohnálek, The evolution of model Rh/ $\text{Fe}_3\text{O}_4(001)$ catalysts in hydrogen environments, *Surf. Sci.*, 2025, **751**, 122617.

45 M. A. Sharp, C. J. Lee, M. Mahapatra, B. D. Kay and Z. Dohnálek, Active Site Evolution during Formic Acid Conversion on Rh-Substituted $\text{Fe}_3\text{O}_4(001)$, *Top. Catal.*, 2025, **68**, 1848–1856.

46 C. Wang, P. Sombut, L. Puntscher, Z. Jakub, M. Meier, J. Pavelec, R. Bliem, M. Schmid, U. Diebold, C. Franchini and G. S. Parkinson, CO-Induced Dimer Decay Responsible for Gem-Dicarbonyl Formation on a Model Single-Atom Catalyst, *Angew. Chem. Int. Ed.*, 2024, **63**, e202317347.

47 J. Hulva, M. Meier, R. Bliem, Z. Jakub, F. Kraushofer, M. Schmid, U. Diebold, C. Franchini and G. S. Parkinson, Unraveling CO adsorption on model single-atom catalysts, *Science*, 2021, **371**, 375–379.

48 D. Rath, V. Mikerásek, C. Wang, M. Eder, M. Schmid, U. Diebold, G. S. Parkinson and J. Pavelec, Infrared reflection absorption spectroscopy setup with incidence angle selection for surfaces of non-metals, *Rev. Sci. Instrum.*, 2024, **95**, 065106.

49 J. Pavelec, J. Hulva, D. Halwidl, R. Bliem, O. Gamba, Z. Jakub, F. Brunbauer, M. Schmid, U. Diebold and G. S. Parkinson, A multi-technique study of CO_2 adsorption on Fe_3O_4 magnetite, *J. Chem. Phys.*, 2017, **146**, 014701.

50 D. Halwidl, *Development of an Effusive Molecular Beam Apparatus*, Springer Fachmedien Wiesbaden, Wiesbaden, 2016.

51 J. I. J. Choi, W. Mayr-Schmöller, F. Mittendorfer, J. Redinger, U. Diebold and M. Schmid, The growth of ultra-thin zirconia films on $\text{Pd}_3\text{Zr}(0001)$, *J. Phys. Condens. Matter*, 2014, **26**, 225003.

52 M. Antlanger, W. Mayr-Schmöller, J. Pavělec, F. Mittendorfer, J. Redinger, P. Varga, U. Diebold and M. Schmid, Pt 3 Zr(0001): A substrate for growing well-ordered ultrathin zirconia films by oxidation, *Phys. Rev. B*, 2012, **86**, 035451.

53 F. J. Giessibl, The qPlus sensor, a powerful core for the atomic force microscope, *Rev. Sci. Instrum.*, 2019, **90**, 011101.

54 G. Kresse and J. Furthmüller, Efficiency of ab-initio total energy calculations for metals and semiconductors using a plane-wave basis set, *Comput. Mater. Sci.*, 1996, **6**, 15–50.

55 G. Kresse and D. Joubert, From ultrasoft pseudopotentials to the projector augmented-wave method, *Phys. Rev. B*, 1999, **59**, 1758–1775.

56 P. E. Blöchl, Projector augmented-wave method, *Phys. Rev. B*, 1994, **50**, 17953–17979.

57 J. P. Perdew, K. Burke and M. Ernzerhof, Generalized Gradient Approximation Made Simple, *Phys. Rev. Lett.*, 1996, **77**, 3865–3868.

58 S. Grimme, S. Ehrlich and L. Goerigk, Effect of the damping function in dispersion corrected density functional theory, *J. Comput. Chem.*, 2011, **32**, 1456–1465.

59 A. Kiejna, T. Ossowski and T. Pabisak, Surface properties of the clean and Au/Pd covered $\text{Fe}_3\text{O}_4(111)$: DFT and DFT + U study, *Phys. Rev. B*, 2012, **85**, 125414.

60 I. Bernal-Villamil and S. Gallego, Charge order at magnetite $\text{Fe}_3\text{O}_4(001)$: surface and Verwey phase transitions, *J. Phys. Condens. Matter*, 2015, **27**, 012001.

61 N. Mina-Camilde, C. Manzanares I. and J. F. Caballero, Molecular Constants of Carbon Monoxide at $v = 0, 1, 2$, and 3: A Vibrational Spectroscopy Experiment in Physical Chemistry, *J. Chem. Educ.*, 1996, **73**, 804.

62 M. Eder, F. J. Lewis, J. I. Hütner, P. Sombut, M. Hao, D. Rath, J. Balajka, M. Wagner, M. Meier, C. Franchini, U. Diebold, M. Schmid, F. Libisch, J. Pavělec and G. S. Parkinson, Multi-Technique Characterization of Rhodium Gem-Dicarbonyls on $\text{TiO}_2(110)$, *arXiv*, 2025, preprint, arXiv:arXiv:2506.21068, DOI: 10.48550/arXiv.2506.21068.

63 G. Bistoni, S. Rampino, N. Scafuri, G. Ciancaleoni, D. Zuccaccia, L. Belpassi and F. Tarantelli, How π back-donation quantitatively controls the CO stretching response in classical and non-classical metal carbonyl complexes, *Chem. Sci.*, 2016, **7**, 1174–1184.

64 F. C. Meunier, Relevance of IR Spectroscopy of Adsorbed CO for the Characterization of Heterogeneous Catalysts Containing Isolated Atoms, *J. Phys. Chem. C*, 2021, **125**, 21810–21823.

65 N. G. Petrik and G. A. Kimmel, Adsorption Geometry of CO versus Coverage on TiO₂(110) from s- and p-Polarized Infrared Spectroscopy, *J. Phys. Chem. Lett.*, 2012, **3**, 3425–3430.

66 K. I. Hadjiivanov and G. N. Vayssilov, in *Advances in Catalysis*, Academic Press, 2002, vol. 47, pp. 307–511.

67 G. S. Parkinson, T. A. Manz, Z. Novotný, P. T. Sprunger, R. L. Kurtz, M. Schmid, D. S. Sholl and U. Diebold, Antiphase domain boundaries at the Fe₃O₄(001) surface, *Phys. Rev. B*, 2012, **85**, 195450.

68 O. Gamba, J. Hulva, J. Pavelec, R. Bliem, M. Schmid, U. Diebold and G. S. Parkinson, The Role of Surface Defects in the Adsorption of Methanol on Fe₃O₄(001), *Top. Catal.*, 2017, **60**, 420–430.

69 M. A. Albrahim, A. Shrotri, R. R. Unocic, A. S. Hoffman, S. R. Bare and A. M. Karim, Size-Dependent Dispersion of Rhodium Clusters into Isolated Single Atoms at Low Temperature and the Consequences for CO Oxidation Activity, *Angew. Chem.*, 2023, **135**, e202308002.

70 A. H. Jenkins, E. E. Dunphy, M. F. Toney, C. B. Musgrave and J. W. Medlin, Tailoring the Near-Surface Environment of Rh Single-Atom Catalysts for Selective CO₂ Hydrogenation, *ACS Catal.*, 2023, **13**, 15340–15350.

71 J. Hulva, Z. Jakub, Z. Novotny, N. Johansson, J. Knudsen, J. Schnadt, M. Schmid, U. Diebold and G. S. Parkinson, Adsorption of CO on the Fe₃O₄(001) Surface, *J. Phys. Chem. B*, 2018, **122**, 721–729.

72 E. Şaşioğlu, C. Friedrich and S. Blügel, Effective Coulomb interaction in transition metals from constrained random-phase approximation, *Phys. Rev. B*, 2011, **83**, 121101.

73 G. Lan, J. Song and Z. Yang, A linear response approach to determine Hubbard *U* and its application to evaluate properties of Y₂B₂O₇, B = transition metals 3d, 4d and 5d, *J. Alloys Compd.*, 2018, **749**, 909–925.

74 R. Tesch and P. M. Kowalski, Hubbard *U* parameters for transition metals from first principles, *Phys. Rev. B*, 2022, **105**, 195153.

Supporting Information

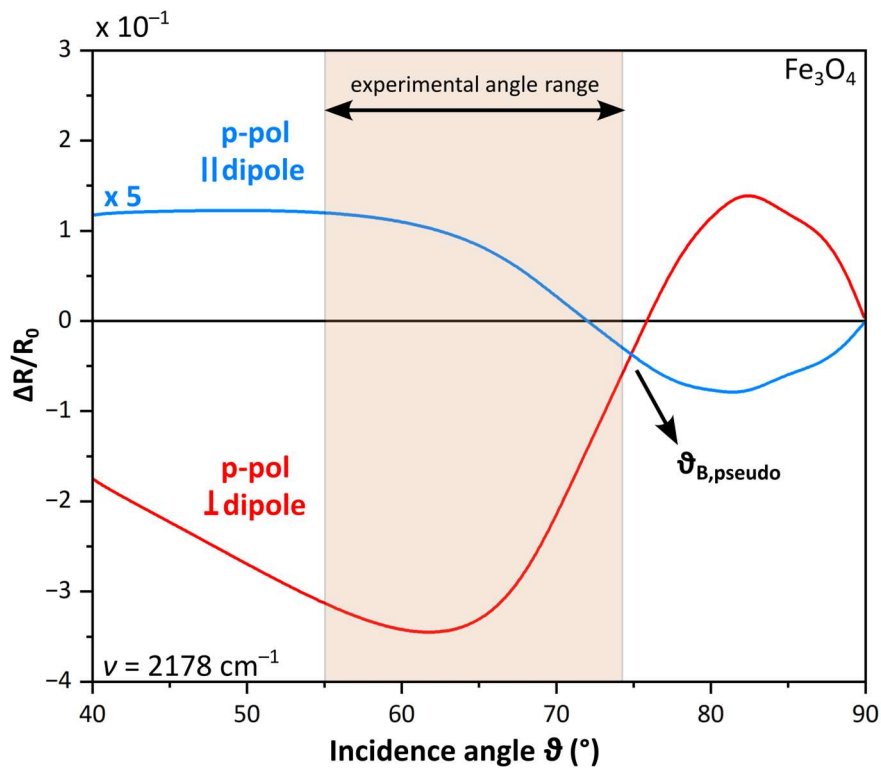


Figure S1. Normalised reflectivity difference $\Delta R/R_0$ for an adsorbate on Fe_3O_4 at a representative frequency of $\nu = 2178 \text{ cm}^{-1}$, including system-specific corrections. $\Delta R/R_0$ was calculated using a linewidth of $\gamma = 6 \text{ cm}^{-1}$, a static electronic polarisability $\alpha_e = 0$, and a vibrational polarisability $\alpha_v = 3.4 \times 10^{-26} \text{ cm}^3$. The calculation includes corrections for an incidence-angle spread of $\kappa = \pm 2^\circ$, a system-specific depolarisation factor $\Gamma = 0.21$, and the contribution from vicinity illumination.^{1,2} The red curve shows the response for p-polarised light interacting with a dipole moment perpendicular to the surface, while the blue curve corresponds to p-polarised light with a dipole moment parallel to the surface and lying in the plane of incidence (scaled by a factor of 5 for clarity). The beige region indicates the incidence-angle range used in our experiments (55° – 74°), which lies below the pseudo-Brewster angle where the characteristic band inversion occurs. Within this range, perpendicular dipoles give rise to strong negative peaks, whereas parallel dipoles yield much weaker positive features—approximately fifteen times smaller in magnitude. The signal in p-polarisation vanishes for a dipole moment normal to the angle of incidence. Since the azimuthal orientation of alternating (001) planes of $\text{Fe}_3\text{O}_4(001)$ changes by 90° , only half of the molecules with a given azimuthal orientation with respect to the Fe rows contribute to the signal. This results in a 30-fold increase in peak height between out-of-plane and in-plane dipole moments.

Table S1. Relative increase in IRAS peak intensities between 0.2 ML and 0.4 ML Rh/Fe₃O₄(001)

Peak Position	Peak height (0.2 ML Rh)	Peak height (0.4 ML Rh)	Relative increase
1979	-5.4×10^{-4}	-7.9×10^{-4}	≈ 1.5
2037	-8.8×10^{-5}	-3.8×10^{-4}	≈ 4.3
2059	-5.9×10^{-5}	-3.0×10^{-4}	≈ 5.1

The table summarises the change in IRAS peak intensities between Rh coverages of 0.2 ML (black spectrum in Fig.2) and 0.4 ML (blue spectrum in Fig.2). The band at 1979 cm⁻¹, associated with CO bound to twofold coordinated Rh₁ sites, increases by a factor of ≈ 1.5 . In comparison, the gem-dicarbonyl symmetric stretch at 2037 cm⁻¹ increases by a factor of ≈ 4.3 , and the band at 2059 cm⁻¹ attributed to CO adsorption on fivefold coordinated Rh₅-fold sites increases by a factor of ≈ 5.1 . The substantially larger relative increases of the higher-frequency bands further support their assignment to gem-dicarbonyl species and CO bound to fivefold Rh₁ sites.

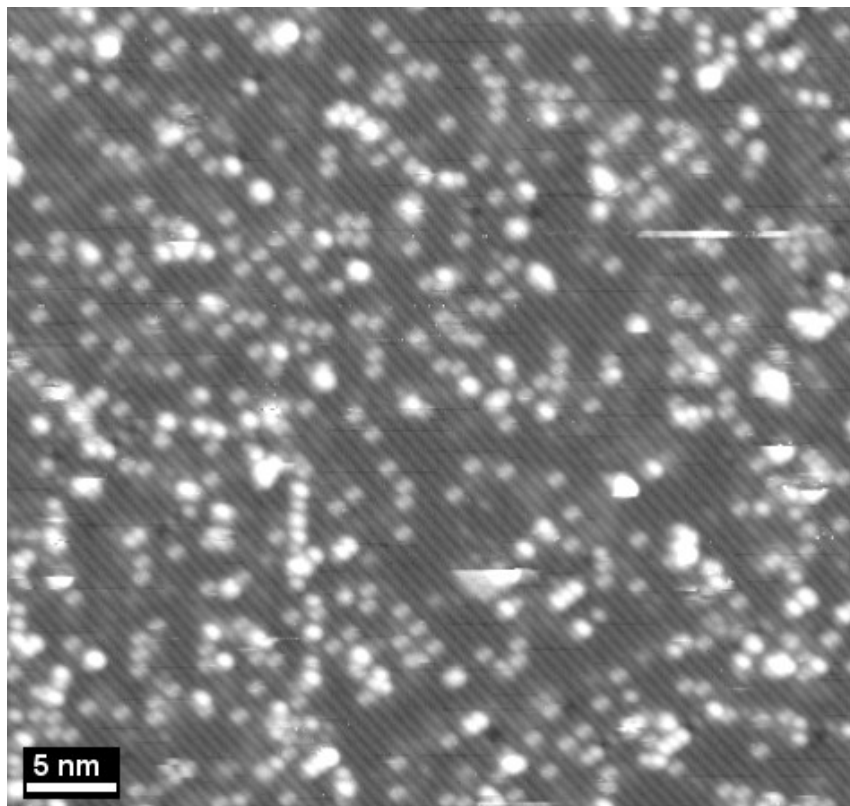


Figure S2. STM measurement of CO adsorption on Rh/Fe₃O₄(001). This STM image was acquired under UHV conditions following the NAP-STM measurement of Rh/Fe₃O₄(001) in 2 mbar CO shown in Figure 5a. The dicarbonyl species formed during CO exposure remain stable even under UHV, consistent with the thermodynamic stability predicted by DFT (adsorption energy: -2.21 eV per CO). The few clusters or blurry features visible in the image may arise from minor contamination deposited during the prolonged CO exposure at 2 mbar.

References

- 1 D. Rath, Infrared Reflection Absorption Spectroscopy with Angle Selection, Technische Universität Wien, 2024.
- 2 D. Rath, V. Mikerásek, C. Wang, M. Eder, M. Schmid, U. Diebold, G. S. Parkinson and J. Pavelec, *Rev. Sci. Instrum.*, 2024, **95**, 065106.